Applied Computational Electromagnetics Society

Express Journal

June 2016 Vol. 1 No. 6

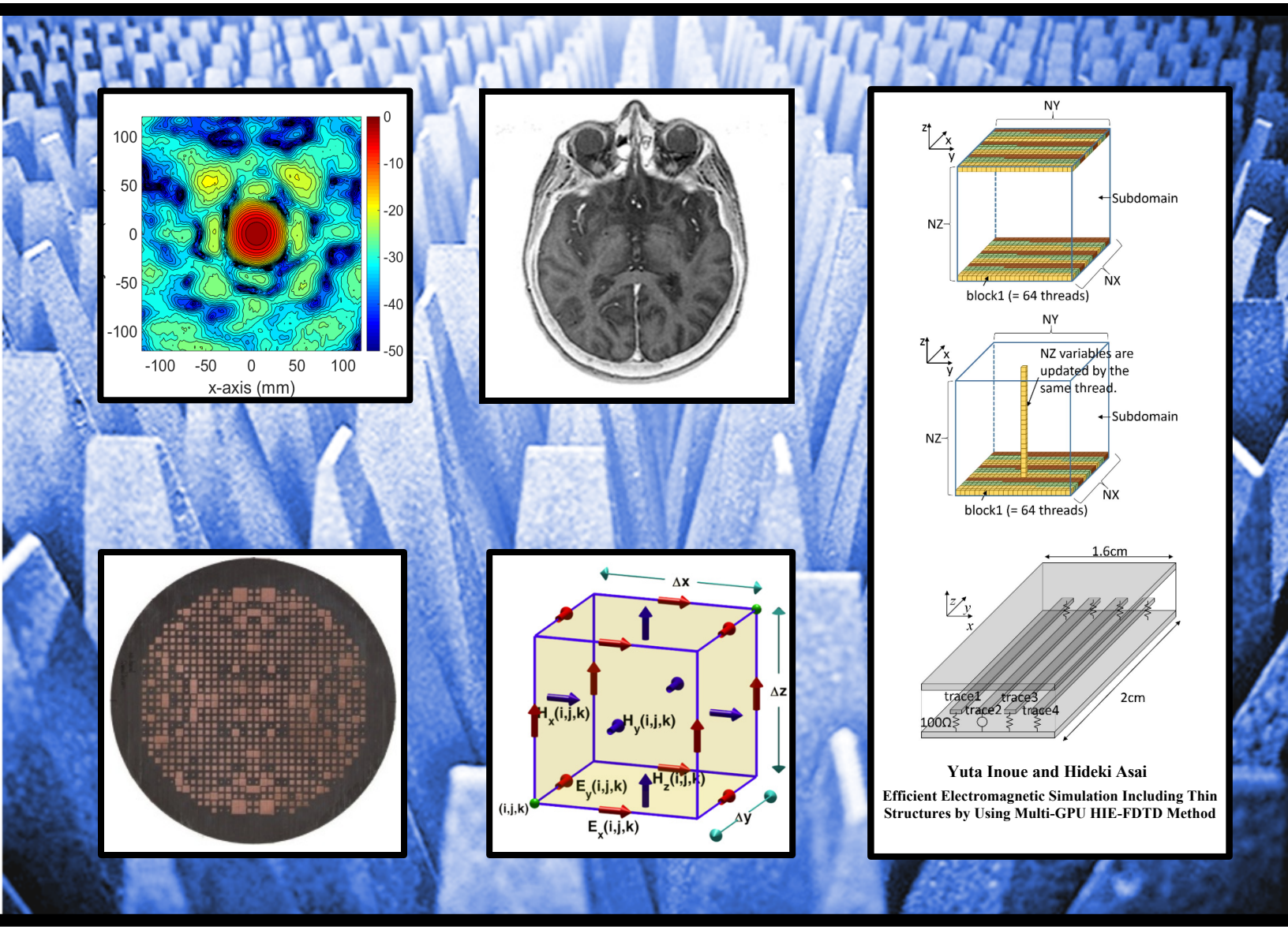

Yuta Inoue and Hideki Asai

Efficient Electromagnetic Simulation Including Thin Structures by Using Multi-GPU HIE-FDTD Method

APPLIED COMPUTATIONAL ELECTROMAGNETICS SOCIETY EXPRESS JOURNAL

http://aces-society.org

GENERAL INFORMATION

PURPOSE AND SCOPE: The Applied Computational Electromagnetics Society ***(ACES) Express*** Journal hereinafter known as the ***ACES Express Journal*** is devoted to the timely and rapid exchange of information in computational electromagnetics, to the advancement of the state-of-the art, and the promotion of related technical activities. The primary objective of the information exchange is to inform the scientific community in a short amount of time on the developments of recent computational electromagnetics tools and their use in electrical engineering, physics, or related areas. The technical activities promoted by this publication include code validation, performance analysis, and input/output standardization; code or technique optimization and error minimization; innovations in solution technique or in data input/output; identification of new applications for electromagnetics modeling codes and techniques; integration of computational electromagnetics techniques with new computer architectures; and correlation of computational parameters with physical mechanisms.

SUBMISSIONS: The ***ACES Express Journal*** welcomes original, previously unpublished papers, relating to applied computational electromagnetics. Typical papers will represent the computational electromagnetics aspects of research in electrical engineering, physics, or related disciplines as well as research in the field of applied computational electromagnetics.

Manuscripts are to be submitted through the upload system of ***ACES*** web site http://aces-society.org Please see "Information for Authors" on inside of back cover and at ***ACES*** web site. For additional information contact the Editor-in-Chief:

Dr. Ozlem Kilic
Department of Electrical Engineering and Computer Science
The Catholic University of America
Washington, DC 20064
Email: kilic@cua.edu

SUBSCRIPTIONS: All members of the Applied Computational Electromagnetics Society are entitled to access and download the ***ACES Express Journal*** of any published journal article available at http://aces-society.org. ***ACES Express Journal*** is an online journal and printed copies are not available. Subscription to ACES is through the web site.

LIABILITY. Neither ***ACES***, nor the ***ACES Express Journal*** editors, are responsible for any consequence of misinformation or claims, express or implied, in any published material in an ***ACES Express Journal*** issue. This also applies to advertising, for which only camera-ready copies are accepted. Authors are responsible for all information contained in their papers. If any material submitted for publication includes material which has already been published elsewhere, it is the author's responsibility to obtain written permission to reproduce such material.

THE APPLIED COMPUTATIONAL ELECTROMAGNETICS SOCIETY EXPRESS JOURNAL

Vol. 1 No. 6 June 2016

TABLE OF CONTENTS

Efficient Electromagnetic Simulation Including Thin Structures by Using Multi-GPU HIE-FDTD Method

Yuta Inoue and Hideki Asai

Research Institute of Electronics
Shizuoka University, Hamamatsu, 432-8561, Japan
inoue.yuta@shizuoka.ac.jp, asai.hideki@shizuoka.ac.jp

Abstract ─ This paper describes an efficient simulation method to solve the large scale electromagnetic problems with thin unit cells in the finite-difference time-domain (FDTD) simulation. The proposed method is based on the hybrid implicit-explicit and multi-GPU techniques, which can choose a larger time step size than that in the conventional one, and using the multiple graphic processing units (GPUs). In the proposed method, the computational time is significantly reduced.

Index Terms ─ Electromagnetic simulation, FDTD method, multi-GPU, time domain analysis.

I. INTRODUCTION

The finite-difference time-domain (FDTD) [1] method is one of the numerical simulation techniques for solving the electromagnetic problems. The FDTD method is a conditionally stable method. Therefore, the maximum time step size is constrained by the Courant-Friedrichs-Lewy (CFL) condition. If the time step size is not satisfied with the CFL condition, the FDTD method becomes unstable. For the analysis of the large scale electromagnetic problems with thin structures such as printed circuit boards, the time step size must be small and it can make the FDTD simulation a huge time consuming task. Thus, the efficient electromagnetic simulation technique is strongly demanded for the efficient designs. In order to overcome the CFL condition problem, the several unconditionally stable methods have been proposed for an arbitrary time step size [1], [2]. However, these methods are unsuitable for the parallel implementation because several overheads degrade the efficiency of parallel computing.

In order to alleviate the CFL condition problem, the hybrid implicit-explicit (HIE)-FDTD method has been proposed and studied for the fast electromagnetic simulation with thin unit cells in the FDTD simulation [3]-[7]. The HIE-FDTD method can adopt a larger time step size than that for the conventional FDTD method. The implicit technique is employed partially, and the computational domain can be easily divided for the parallel computing. Therefore, the message passing interface (MPI)-based parallel-distributed HIE-FDTD method [6] and the general purpose computing on graphic processing unit (GPGPU) based massively parallel HIE-FDTD method [7] have been proposed for the efficient simulation. However, the parallel distributed HIE-FDTD method is required to be faster since CPU is slower than the graphic processing unit (GPU). On the other hand, the memory size of the GPU boards is not sufficient for the large scale problems. Hence, the combination of the MPI based method and the GPGPU based method is demanded for solving the large scale problems. As a result, the proposed method can solve the large scale problems and can reduce the elapsed time drastically from MPI-based and single GPU-based method.

In this paper, the multi-GPU based HIE-FDTD method with MPI and CUDA is proposed for the efficient electromagnetic simulation of the object with thin structures. First, the HIE-FDTD method is reviewed briefly. Next, the proposed method is described. Finally, the efficiency of the proposed method is evaluated through several FDTD simulations.

II. HIE-FDTD METHOD

The HIE-FDTD method [4] has been proposed for the efficient 3-D electromagnetic simulation of the given object with thin unit cells in the FDTD-based computational domain. Here, it is assumed that the given object has the fine scale dimension in the *z* direction such as printed circuit boards. In such a case, the updating formulas of the HIE-FDTD method consist of the two explicit equations which do not contain the derivatives with respect to *z* direction and four implicit equations which include the derivatives with respect to *z* direction. The updating formulas are described in [6].

The updating procedures of the HIE-FDTD method are partially different from the conventional FDTD method. First, E_z and H_z are explicitly updated. Next, E_x and E_y are updated by numerical solution method of simultaneous linear equations such as LU decomposition

Submitted On: September 17, 2015
Accepted On: July 15, 2016

method. After updating E_x and E_y, H_x and H_y are explicitly updated.

The CFL condition of the HIE-FDTD method is alleviated than that of the conventional FDTD method, which is given by:

$$\Delta t_{FDTD} \le \frac{1}{c\sqrt{\Delta x_{\min}{}^{-2} + \Delta y_{\min}{}^{-2} + \Delta z_{\min}{}^{-2}}}, \quad (1)$$

where Δt_{FDTD} is maximum time step size for the conventional FDTD method, c is the speed of light, $\Delta x_{\min}$, $\Delta y_{\min}$ and $\Delta z_{\min}$ are minimum cell sizes along the x, y, and z direction in the computational domain. The CFL condition of the HIE-FDTD method is determined as follows:

$$\Delta t_{HIE} \le \frac{1}{c\sqrt{\Delta x_{\min}{}^{-2} + \Delta y_{\min}{}^{-2}}}, \quad (2)$$

where Δt_{HIE} is maximum time step size for the HIE-FDTD method. From (2), the Δz is removed from the CFL condition of the HIE-FDTD method. Therefore, the time step size can choose the larger time step size than that for the conventional FDTD method. In the case of thin cell along with z direction, the HIE-FDTD method can efficiently simulate.

III. MULTI-GPU HIE-FDTD METHOD

The multi-GPU HIE-FDTD method is combination of the parallel distributed HIE-FDTD method and the GPGPU HIE-FDTD method. In the proposed method, the arithmetic operations are performed by a GPU instead of a CPU. In order to employ multi GPUs, the proposed method uses the three types of domain decomposition techniques. One is the domain decomposition technique for allocating a GPU to a subdomain. The others are the domain decomposition techniques for the GPU computing. In this section, the domain decomposition techniques and updating procedure are described. Here, the MPI library is employed for network communication between the neighboring subdomains and the CUDA is done for the GPU computing.

A. Domain decomposition

First, the domain decomposition technique for allocating a GPU to a subdomain is described. In the proposed method, the whole 3D spatial domain is divided into the several subdomains along the x and y directions. The number of subdomains is same as the number of GPUs. Note that the boundary cells of subdomain are overlapped with the neighboring subdomains. The overlapping boundary cells are employed to communicate magnetic components between the neighboring subdomains. Furthermore, the dummy cells are added to each subdomain in order to correct the total number of cells of x-y plane to a multiple of 64. The dummy cells are employed for the GPU computing. In the updating process, the electromagnetic components at the dummy cells are not updated.

Next, the domain decomposition techniques for GPU computing are shown. The partitioned subdomains for GPU computing are illustrated in Fig. 1. Here, NX, NY, and NZ are the numbers of cells for the x, y, and z directions, respectively. In the proposed method, the domain decomposition techniques are different in the explicit updating procedure and the implicit updating procedure. Figure 1 (a) shows the divided subdomain for explicit updating procedure. The subdomain is partitioned by the blocks which are composed of the 64 threads. A cell is allocated to a thread and is updated by the thread. The thread is smallest element of the process. Therefore, in the explicit updating procedure, the subdomain is divided into (NX×NY×NZ)/64 blocks. On the other hand, the domain decomposition technique for implicit updating procedure is illustrated in Fig. 1 (b). In the implicit updating procedure, x-y plane of the sub-domain is partitioned by the blocks. Thus, each block is assigned to 64×NZ cells. Each thread in the block is allocated to the NZ cells. These cells are updated by using the LU decomposition method [8].

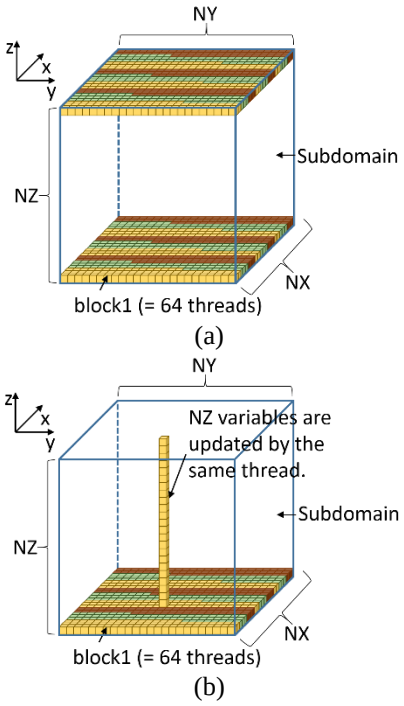

Fig. 1. The domain decomposition and block structure for GPU computing. (a) Domain decomposition for explicit updating procedure, and (b) domain decomposition for implicit updating procedure.

B. Updating procedure

In the proposed method, two types of updating procedures are employed. One is the updating procedure which invokes the blocking data communication

function. The other is the updating procedure which calls the nonblocking data communication function. In the case of invoking the blocking data communication function, each magnetic component at boundary cells is communicated after updating each magnetic component. On the other hand, in the case of calling the nonblacking data communication function, the updating process is divided into two parts. One is the boundary part. The other is except the boundary part. Figure 2 shows the pseudo-code of updating procedure for calling the nonblocking data communication function. From Fig. 2, the data communication and the computation is over lapped by the nonblocking data communication function. Therefore, it is efficiently performed than invoking the blocking data communication function.

```
Transient()
{
  COMMUNICATE Hx and Hy of boundary part
between neighboring subdomains
  WHILE Current Time < Ending Time
    COMPUTE Hz of the boundary part
    COMMUNICATE Hz of boundary part between
     neighboring subdomains
    COMPUTE Hz except boundary part
    COMPUTE Ez except boundary part
    WAIT for completion of Hx and Hy of boundary
     part communicate
    COMPUTE Ez of boundary part
    COMPUTE Ex and Ey except boundary part
    WAIT for completion of Hz of boundary part
     communicate
    COMPUTE Ex and Ey of boundary part
    COMPUTE Hx and Hy of boundary part
    COMMUNICATE Hx and Hy of boundary part
     between neighboring subdomains
  ENDWHILE
}
```

Fig. 2. Pseudo-code of the proposed method.

IV. NUMERICAL RESULTS

First, in order to estimate the accuracy of the proposed method, the simulation has been performed for multi conductor transmission lines illustrated in Fig. 3. Each transmission line is terminated with the resistor (100 Ω). The voltage source is appended to the near end of the trace2. A pulse excitation with 0.5×10^{-9} sec rise/fall time, a width 4×10^{-9} sec, a period 1×10^{-8} sec, and an amplitude 3.3V was used. Mur's first order absorbing boundary condition is used for the absorbing boundary condition. The computational domain consists of 46×40×50 cells and discretized by nonuniform meshes. The minimum cell sizes are Δx=0.2mm, Δy=1 mm, Δz=0.01 mm, respectively. The time step size is 3.33×10^{-14} sec in the FDTD method and 6.53×10^{-13} sec in the HIE-FDTD method. All of the simulations are performed by PC cluster, which is composed of two PCs. These PCs are connected by the gigabit Ethernet. Each PC has an Intel Xeon E5-2650 2GHz and four GPU boards, which are Tesla C2075. Tesla C2075 is one of the GPU boards for the high performance computing. In this simulation, the Intel Xeon E5-2650 was used for the FDTD method and the HIE-FDTD method and eight GPU boards were used for the proposed method. Open MPI is employed for MPI library. Figure 4 shows waveform results of the far end of the trace2 and the trace3. From Fig. 4, the waveform results show good agreement between these methods.

Next, in order to verify the efficiency of the proposed method, the large scale problem has been performed. The number of cells is 1270×1270×102 cells. The minimum cell sizes are Δx=Δy=1 mm, Δz=0.01 mm. Mur's first order absorbing boundary condition is adopted. The time step size for the FDTD method is 3.33×10^{-14} sec. That for the HIE-FDTD method is 1.89×10^{-12} sec. Table 1 shows the simulation results, which are the elapsed time and the speed up ratio, by the FDTD method, the multi-GPU FDTD method, the HIE-FDTD method and the proposed method. The proposed method is performed with single precision floating point and double precision floating point. The peak performance of the Tesla C2075 by using the single precision floating point is two times faster than the peak performance by using the double precision floating point. In the bracket, the communication time is described. From Table 1, the proposed method is about 4000 times faster than the FDTD method by using the 8 GPUs with single precision floating point.

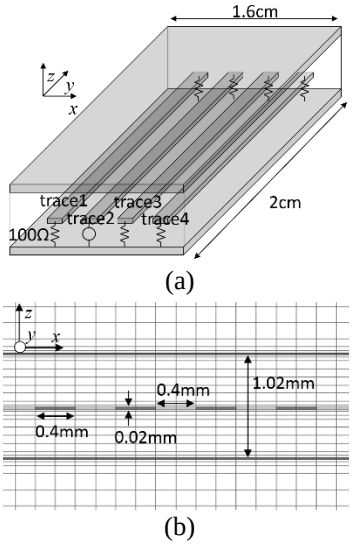

Fig. 3. Example printed circuit board: (a) overhead view of the example circuit, and (b) cross section view of the example circuit.

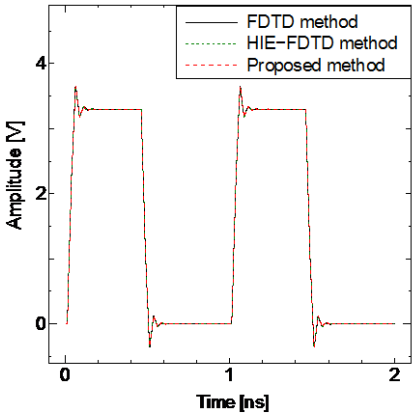

(a)

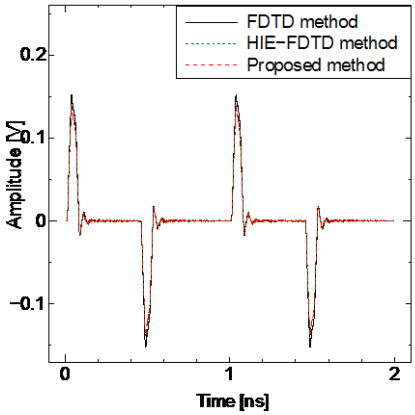

(b)

Fig. 4. Waveform results: (a) far end of the trace2, and (b) far end of the trace3.

Table 1: Elapsed time and speed up ratio

	Elapsed Time (sec)	Speed up Ratio (vs FDTD Method)
FDTD method	499395.0	1.00
Multi-GPU FDTD method	6189.88	80.68
HIE-FDTD method	15110.43	33.05
Proposed method (double precision and blocking)	287.39 [221.23]	1737.69
Proposed method (single precision and blocking)	145.62 [117.33]	3429.44
Proposed method (double precision and nonblocking)	244.86	2039.51
Proposed method (single precision and nonblocking)	126.64	3943.42

V. CONCLUSION

The multi-GPU HIE-FDTD method proposed for the efficient simulation of the large-scale electromagnetic problems including thin structures. In the case of suitable given objects for the HIE-FDTD method, it has been verified that the proposed method is more than about 4000 times faster than the conventional FDTD method in the case of using 8 GPUs with single precision floating point.

ACKNOWLEDGMENT

This work was supported by JSPS KAKENHI Grant Number 24300018.

REFERENCES

[1] A. Taflove and S. C. Hagness, *Computational Electrodynamics: The Finite-Difference Time-Domain Method*. Artech House, Inc., Norwood, 2005.

[2] Y. Yang, R. S. Chen, and E. K. N. Yung, "The unconditionally stable Crank-Nicolson FDTD method for three-dimensional Maxwell's equations," *Microw. Opt. Tech. Lett.*, vol. 48, no. 8, pp. 1619-1622, May 2006.

[3] J. Chen and J. Wang, "A three-dimensional semi-implicit FDTD scheme for calculation of shielding effectiveness of enclosure with thin slots," *IEEE Trans. Electromagn. Compat.*, vol. 49, no. 2, pp. 354-360, May 2007.

[4] M. Unno and H. Asai, "HIE-FDTD method for hybrid system with lumped elements and conductive media," *IEEE Microw. Wireless Compon. Lett.*, vol. 21, no. 9, pp. 453-455, Sep. 2011.

[5] H. Muraoka, Y. Inoue, T. Sekine, and H. Asai, "A hybrid implicit-explicit and conformal (HIE/C) FDTD method for efficient electromagnetic simulation of nonorthogonally aligned thin structures," *IEEE Trans. Electromagn. Compat.*, vol. 57, no. 3, pp. 505-512, June 2015.

[6] Y. Inoue and H. Asai, "Fast fullwave simulation based on parallel distributed HIE-FDTD method," *IEEE APMC 2012*, Kaohsiung, Taiwan, pp. 1253-1255, Dec. 2012.

[7] M. Unno, S. Aono, and H. Asai, "GPU-based massively parallel 3-D HIE-FDTD method for high-speed electromagnetic field simulation," *IEEE Trans. Electromagn. Compat.*, vol. 54, no. 4, pp. 912-921, Aug. 2012.

On The Beam Forming Characteristics of Linear Array Using Nature Inspired Computing Techniques

Suraya Mubeen [1*], A. M. Prasad [2], and A. Jhansi Rani [3]

[1] Department of ECE, JNTU Kakinada, Kakinada-533001, Andhra Pradesh, India
Suraya418@gmail.com

[2] Department of ECE, JNTU Kakinada, Kakinada-533001, Andhra Pradesh, India
a_malli65@yahoo.com

[3] Department of ECE, VR. Siddhartha College of Engineering, Vijayawada-520001, Andhra Pradesh, India
jhansi9rani@gmail.com

Abstract — Beamforming is a serious problem in wireless communication. Many deterministic and numerical techniques are proposed to achieve beamforming. However, the application of evolutionary computing techniques produced better results over many existing conventional methods. In this paper, one such attempt of applying a novel nature-inspired technique known as Firefly algorithm (FFA) to demonstrate beamforming in linear arrays and compared with particle swarm optimization (PSO). The desired objectives of the synthesis process are defined as sidelobe level (SLL) suppression and null positioning. The optimal set of amplitude distribution for the elements in the linear array is obtained using the technique in order to achieve the desired objectives. The results are evaluated in terms of radiation pattern plots.

Index Terms — Antenna array, Firefly algorithm, particle swarm optimization.

I. INTRODUCTION

Beamforming, on one hand it involves in observing deep nulls in the direction of the undesired signal and, on the other hand, it involves in positioning the main beam in the direction of the desired signal. Antenna array which have perfect control of radiation characteristics like sidelobe level (SLL), control on beam width (BW) along with beam steering (BS) capabilities have emerged as the best candidates for beamforming applications [1]. Linear arrays are the simplest form of array antenna geometry. All the elements of the array are oriented along a straight line defined in terms of array length and number of elements. These linear arrays are the best candidates for beamforming applications with efficient sidelobe level suppression [2-4] and null control [5] characteristics. These arrays are capable of interference suppression through beam-forming technique. Nulls are located in the direction of arrival (DOA) of the interference signal while the main beam is steered to the DOA of the desired signal in order achieve the above said characteristics. Many conventional techniques are proposed to solve the problem of beamforming. Unfortunately, these are time-consuming as well as provide poor performance. In order to overcome these hurdles, in the recent past several evolutionary techniques are proposed [3-6]. These techniques are quite efficient and often express the supremacy over traditional techniques.

In this paper, novel nature-inspired metaheuristic evolutionary computing algorithm known as Firefly algorithm (FFA) [6, 7] is employed to achieve the specified two objectives of SLL suppression and null position in linear arrays. The rest of the paper is organized as follows. Sections 2 and 3 are dedicated to description of the problems statement and formulation of cost function. Implementation of the algorithm for the proposed problem is given in Section 3. The case wise presentation of results is given in Section 4 which is followed by overall conclusion in Section 5.

II. PROBLEM STATEMENT

The problem statement can be considered as to determine the amplitude distribution of linear array which produces the desired radiation pattern. The geometry of the broadside linear array of N equi-spaced isotropic elements with symmetric excitation positioned along Z-axis is shown in Fig. 1.

Mathematically, the array factor can be stated as:

$$E(\theta) = \sum_{n=1}^{N} I_n \exp\left[j(n-1)\left(kd\cos\theta + \beta\right)\right]. \qquad (1)$$

Here, x_n is Amplitude of excitation of the nth element of the array, k is wave number, d is spacing between the elements ($\lambda/2$), $\beta = kd\cos\theta_d$ and θ_d = Scan angle and

Submitted On: February 10, 2016
Accepted On: August 17, 2016

N = Number of elements in the array. Progressive phase β is zero as pattern maxima is directed towards $\theta_d = 90^0$ for broadside linear array. However, in scanned array pattern maxima is oriented at an angle θ_d .

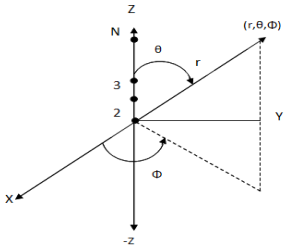

Fig.1. Geometry of broadside linear array.

III.COST FUNCTION FORMULATION

The two objectives considered in this work corresponding to linear array synthesis are SLL suppression and null positioning. The cost functions corresponding to these two objectives are given as below.

For SLL optimization:

$$f1 = \max[E_{\Theta=FN \text{ to } \pi/2}]$$

$$cf1 = |f1-40| \quad \text{if } f1<40$$
$$= 0 \quad \text{otherwise,} \qquad (2)$$

where cf1 is cost function and FN is first null.

For null positioning:

$$E_{nmax} = \max[E_{(\Theta=n1)}, E_{(\Theta=n2)}, E_{(\Theta=n3)}]$$

$$cf2 = |E_{nmax}-60| \quad \text{if } E_{nmax}<60$$
$$= 0 \quad \text{otherwise,} \qquad (3)$$

where n1, n2 and n3 are desired null positions in degrees.

IV. OPTIMIZATION ALGORITHMS

A. Firefly algorithm

Genesis

FFA is proposed by Yang [6]. Like several other swarm intelligence based algorithms, FFA is also inspired by the natural behaviour of fireflies and the phenomenon of bioluminescent communication. Firefly species produce short and rhythmic flashes. These flashes of light play a vital role in bioluminescent communication. Mostly the flash pattern is unique for every species in terms of frequency, colour and time for which the flash of light is generated. These patterned flashes are used by the fireflies to attract other fireflies for mating. According to inverse square law the intensity of light at a certain distance r from the light source. Which means that the intensity of the light I goes on decreasing as the distance r increase in terms of $I \alpha 1/r^2$. In addition to this another phenomenon known as absorption, the light becomes weaker as it travels along the distance. Due to these factors when combined make most fireflies visible at a limited distance, normally to a few hundred meters at night, which is quite enough for fireflies to communicate with each other. The following are the rules that are used to describe the structure of the FFA:

1) All fireflies are unisex so that one firefly will be attracted to other fireflies regardless of their sex.
2) Attractiveness depends on the brightness of the flashed light. Accordingly, firefly with brighter flash is supposed to have good attractiveness than the firefly with less brightness.
3) Brightness is defined by the objective function or the landscape of the species.

Algorithm Construction

The construction of the algorithm considers several base rules which mimic the actual behaviour of the fireflies. It is interesting to note that these fireflies (FF) are unisex and are capable of drawing the attention of any companion FF. The degree of attraction is referred as individual's brightness. The brightness or light intensity of a firefly is influenced by the landscape of fitness/cost function. The basic steps of the FA can be summarized as the pseudo code in Fig. 2.

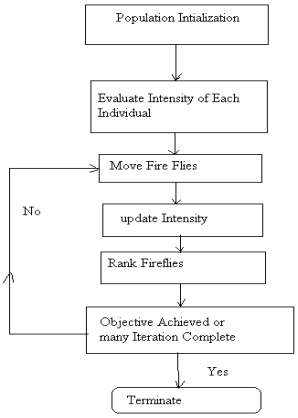

Fig. 2. Flowchart of Firefly algorithm.

Implementation of FFA for LA Synthesis

The adoption of the algorithm for the array synthesis problem starts with population initialization. Every individual FF in the population is considered as a respective array and the amplitude distribution for each array in the population is randomly generated. If P individual FF are considered, then the population is a vector of size 1xK. However, each individual FF is again a vector of size equal to the number of elements in each array. For example, the i^{th} FF is given as follows:

$$x_i = [x_1, x_2, x_3 \ldots x_K], \qquad (4)$$

Similarly, the population matrix is given as:

$$X = \begin{bmatrix} x_1 \\ x_2 \\ . \\ . \\ x_P \end{bmatrix} = \begin{bmatrix} x_{11}\, x_{12} \ldots . x_{1K} \\ x_{21}\, x_{22} \ldots . x_{2K} \\ . \; . \; . \; . \; . \; . \; . \\ . \; . \; . \; . \; . \; . \; . \\ x_{P1}\, x_{P2} \ldots . x_{PK} \end{bmatrix}. \qquad (5)$$

After the population initialization the immediate step if FF evaluation, which means to evaluate the fitness of the FF and the corresponding amplitude distribution:

$$I_i = \text{ObjFunc}(x_i). \quad (6)$$

The calculation of the attractiveness of an FF is given by:

$$\beta(r) = \beta_o * \exp\left(-\gamma r_{ij}^2\right). \quad (7)$$

Here, r is the distance between any two fireflies, β_o is the initial attractiveness at r=0 and γ is the absorption coefficient which controls the decrease of the light intensity. The distance between any two fireflies i and j at x_i and x_j respectively can be defined as a Cartesian distance 'r_{ij}' using the following equation:

$$r_{ij} = \left|x_i - x_j\right| = \sqrt{\sum_{k=1}^{n}\left(x_{ij} - x_{jk}\right)^2}. \quad (8)$$

The movement of a firefly 'i', which is attracted by a more attractive (i.e., brighter) firefly 'j' is given by the following equation:

$$x_i = x_i + \beta_o * \exp\left(-\gamma r_{ij}^2\right) * \left(x_j - x_i\right) + \alpha * \left(\text{rand} - 1/2\right). \quad (9)$$

B. Particle swarm optimization

PSO is developed by Kennedy and Eberhart and applied to several engineering problems. PSO belongs to the class of population based optimization technique which is inspired by social behaviour of bird flocking or fish schooling. The population in PSO constitutes particles. Each particle refers to the position in the search space. Every particle is subjected to move around the search space in search of the target and updates in every iteration. The displacement is governed by both velocity and position of the particle. The velocity depends on personal best position and the global best position of the particle. Personal best refers to the best position of the particle from the displacement history of the particle, while the global best refers to the best position among the flock in the current iteration. This is mathematically modelled using the following equation:

$$v_{k+1}^i = w v_k^i + \frac{\beta * rand(p^i - x_k^i)}{\Delta t} + \gamma * \frac{rand(p_k^g - x_k^i)}{\Delta t}, \quad (10)$$

$$x_{k+1}^i = x_k^i + \Delta t * v_{k+1}^i$$

v_k^i = velocity of i^{th} particle in the kth iteration, p_k^i = personal best of i^{th} particle in the kth iteration, p_k^g = global best in the kth iteration, w = inertial weight, β and α are cognitive and communal coefficients. In this case both are equal to 0.5.

V. RESULTS AND DISCUSSION

The simulation based experimentation is carried out for two different objectives. As discussed earlier, one of the objective is to obtain very low SLL than uniform distribution under scanned and un-scanned beam conditions. Un-scanned beam refers to position of main beam at 0^0 while scanned beam refers to main beam positioned at 30^0. In both the cases, the SLL is maintained well below the level observed with uniform distribution in which all the elements in the array are uniformly excited. Suppressed SLL to -40 dB is achieved by applying FFA to obtain non-uniform amplitude distribution. The results pertaining to this discussion are mentioned in Fig. 3. The pattern with dashed line refers to uniform distribution where the SLL is -13 dB while the solid line and dotted line refers to un-scanned and scanned radiation patterns with non-uniform distribution using FFA respectively.

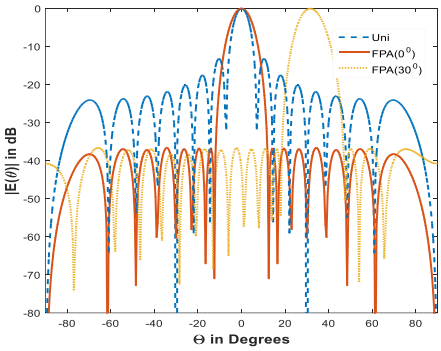

Fig. 3. SLL suppression in unscanned and scanned patterns.

As a second objective the problem of null positioning is considered for both unscanned and scanned beams. As a frst case in this objective, multiple nulls with fixed main position at 0^0 using both PSO and FFA is considered. The DOA of the interference signals are -25^0, 40^0 and 60^0. This is demonstrated in terms of radiation pattern in Fig. 4 (a) and the corresponding convergence plots in Fig. 4 (b). The amplitude distribution obtained using the FFA and PSO is given in the corresponding column of Table 1. As a second case beamsteering along with three nulls is considered. This is shown in the Fig. 5 (a), where the main beam is scanned to an angle of 30^0 which is considered as the DOA of the desired signal. The respective convergence plot is as shown in Fig. 5 (b). The corresponding amplitude distribution using PSO and FFA are as given in Table 1.

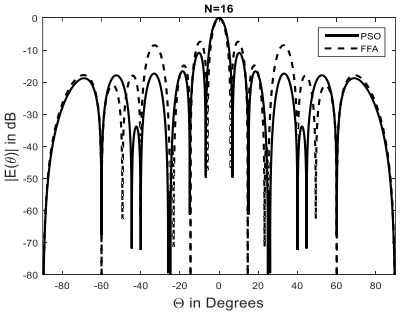

(a)

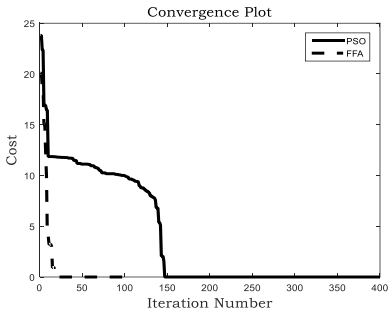

(b)

Fig. 4. (a) Radiation pattern with nulls at -25^0, 40^0 and 60^0 while main beam positioned at 0^0, and (b) convergence plot for PSO and FFA.

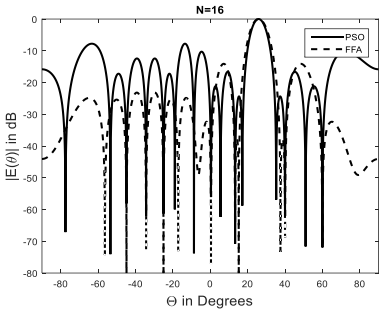

(a)

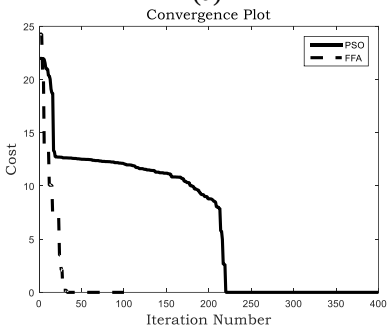

(b)

Fig. 5. (a) Radiation pattern with nulls at -25^0, 40^0 and 60^0 while main beam positioned at 25^0, and (b) convergence plot for PSO and FFA.

Table 1: Amplitude distribution obtained using FFA for different cases

Element Number	Amplitude Distribution					
	Fig. 3		Fig. 4		Fig. 5	
	0^0	30^0	FFA	PSO	FFA	PSO
1&1'	0.76	0.80	0.54	0.76	0.99	0.47
2&2'	0.72	0.76	0.04	0.36	0.86	0.57
3&3'	0.64	0.68	0.11	0.56	0.56	0.14
4&4'	0.53	0.56	0.77	0.75	0.41	0.38
5&5'	0.41	0.44	0.71	0.75	0.48	0.50
6&6'	0.29	0.31	0.46	0.85	0.59	0.13
7&7'	0.18	0.20	0.60	0.55	0.37	0.00
8&8'	0.13	0.15	0.85	0.73	0.38	0.68

VI CONCLUSION

FFA has been successfully applied to array synthesis problems in beamforming applications with multiple objectives. The technique of generating nulls in the desired directions in order to suppress the interference signals is well demonstrated under un-scanned and scanned conditions for beamforming characteristics. FFA has shown its efficiency and simplicity in terms of computation time and complexity. It is evident from the plots that the convergence is achieved earlier with FFA than PSO in all the cases mentioned above. Moreover, the convergence is delayed when the beam is scanned to a certain angle. The technique demonstrated in this paper can easily be extended to any multimodal problems with several constraints.

REFERENCES

[1] S. A. Schelkunoff and H. T. Friis, *Antennas Theory and Practice*. JW & Sons Inc., London, 1952.

[2] K.-K. Yan and Y. Lu, "Sidelobe reduction in array-pattern synthesis using genetic algorithm," *IEEE Transactions on Antennas and Propagation*, vol. 45, no. 7, pp. 1117-1122, 1997.

[3] V. V. S. S. S. Chakravarthy, K. Naveen Babu, S. Suresh, P. Chaya Devi, and P. Mallikarjuna Rao, "Linear array optimization using teaching learning based optimization," *Advances in Intelligent Systems and Computing*, vol. 338, pp. 183-187, 2015.

[4] V. S. S. S. Chakravarthy Vedula, S. R. Chowdary Paladuga, and M. Rao Prithvi, "Synthesis of circular array antenna for sidelobe level and aperture size control using flower pollination algorithm," *International Journal of Antennas and Propagation*, vol. 2015, 2015.

[5] D. Karaboga, K. Guney, and A. Akdagli, "Antenna array pattern nulling by controlling both the amplitude and the phase using modified touring ant colony optimisation algorithm," *Int. Journal of Electronics*, vol. 91, pp. 241-251, 2004.

[6] X.-S. Yang, "Firefly algorithms for multimodal optimization," *in Stochastic Algorithms: Foundations and Applications: 5th International Symposium, SAGA 2009*, Sapporo, Japan, October 26-28, 2009. Proceedings, vol. 5792 of Lecture Notes in Computer Science, pp. 169-178, Springer, Berlin, Germany, 2009.

[7] B. Basu and G. K. Mahanti, "Fire fly and artificial bees colony algorithm for synthesis of scanned and broadside linear array antenna," *Progress In Electromagnetics Research B*, vol. 32, pp. 169-190, 2011.

Bandwidth Enhancement of Dipole Antennas using Parasitic Elements

Garrett Hoch, Atef Elsherbeni, and Payam Nayeri

Department of Electrical Engineering and Computer Science
Colorado School of Mines, Golden, CO 80401, USA
ghoch@mines.edu, aelsherb@mines.edu, pnayeri@mines.edu

Abstract ─ Dipole antennas have a limited bandwidth which restricts their use to narrow bandwidth applications. To improve the functionality of a dipole antenna, additional wire elements can be added to the dipole antenna to increase the impedance matching and bandwidth. A design for a modified dipole antenna is proposed and analyzed using multiple computational electromagnetic software to determine how the additional wire elements affect the input impedance bandwidth and radiated fields. The antenna was then fabricated and tested and compared to simulation results. The modified dipole antenna shows a bandwidth improvement of more than four times, approaching 31%, while maintaining radiation patterns similar to a traditional dipole antenna with slightly higher gain.

Index Terms ─ Antenna, bandwidth, dipole, far field, gain, impedance.

I. INTRODUCTION

Many modern wireless communication systems require antennas that can provide omnidirectional radiation coverage. As such, the classic half-wavelength dipole antenna which provides a uniform omnidirectional coverage is a popular candidate for these systems. The primary drawback for these antennas however is the fact that they operate in a very narrow bandwidth, which limits their application in modern communication systems. In this work, we propose a new configuration for the classic wire dipole antenna, to improve its bandwidth. The presented design is an extension of the configuration proposed in [1]. Four wire elements connected to the wire dipole antenna, as shown in Fig. 1. This essentially creates a quasi-log periodic wire antenna, which minimizes the reactive part of the impedance and improves the matching at the input port of the antenna, resulting in a wider bandwidth. It is shown that by proper tuning of these parasitic wires, the bandwidth of the classic dipole antenna can be increased by more than four times, while maintaining an omnidirectional radiation pattern and slightly increasing the gain.

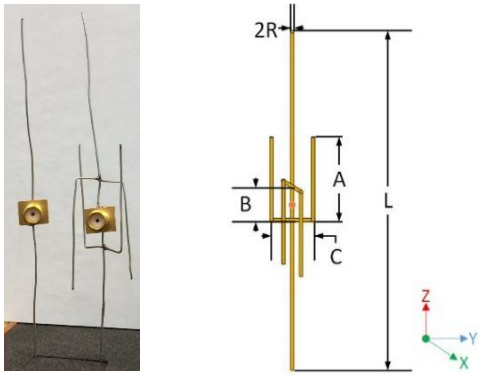

Fig. 1. Dipole antenna models: (left) dipole antenna, (center) modified dipole antenna, and (right) the modified dipole configuration along with design parameters.

II. DESIGN

The initial design for this study is based on the work reported in [1]-[3]. The objective of this study is to further the analysis of the modified dipole antenna configuration shown in Fig. 1. To this end, we compare the performance of the classic wire dipole antenna, with the modified dipole. The analysis is conducted using three computational electromagnetic software: FEKO [4], Ansys HFSS [5], and CEMS [6]. A parametric study for design parameters A, B, and C was conducted using HFSS to understand how the impedance matching of the antenna is effected by the additional wire elements. The parameters R and L were set to 0.2 mm and 128 mm respectively in all used software packages and for the parametric study.

Figures 2-4 show the result of the parametric study. Figure 2 shows the results when varying A with B=10 mm and C = 18 mm. As the length of A increases the real part of the input impedance decreases. The imaginary part of the input impedance curve straightens out as the length of A increases. From the results depicted here, it can be seen that the length of A that corresponds to a real input impedance close to 50 Ohms and an imaginary input impedance around zero, i.e., best matching over a broad frequency range, is for A = 33 mm.

Submitted On: April 26, 2016
Accepted On: July 8, 2016

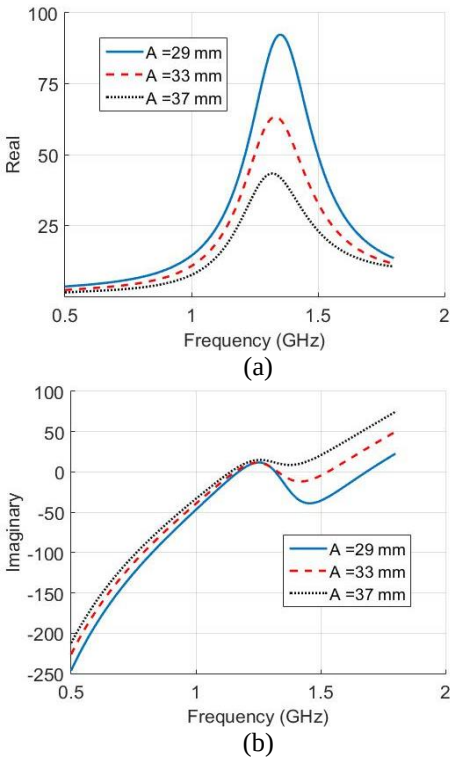

Fig. 2. Input impedance versus frequency: (a) real and (b) imaginary.

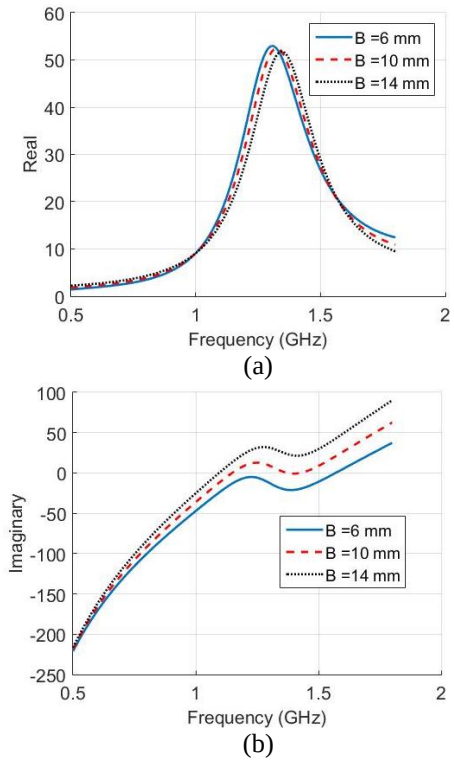

Fig. 3. Input impedance versus frequency: (a) real and (b) imaginary.

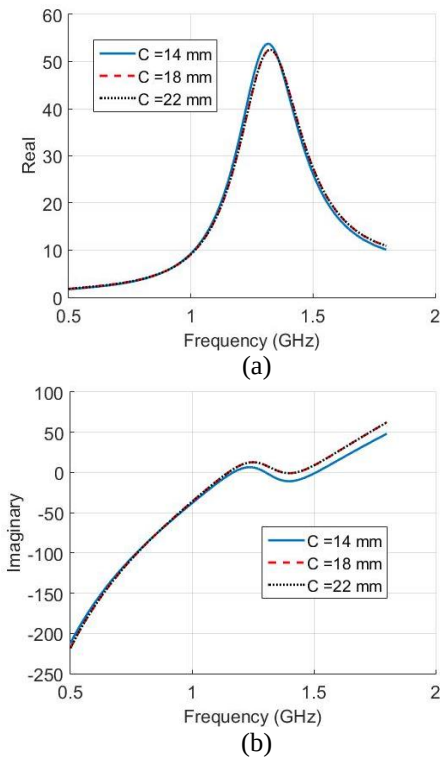

Fig. 4. Input impedance versus frequency: (a) real and (b) imaginary.

Figures 3 and 4 show the parametric study results for B and C. For the parametric study with B, A = 33 mm and C = 18 mm. For the parametric study with C, A = 33 mm and B = 10 mm. Parameters B and C show similar behaviors as for A, but to less extent. From the study reported here it can be seen that A is the main tuning parameter for impedance matching in this modified dipole configuration. The dimensions of the design parameters were chosen based on the results reported here and are A = 33 mm, B = 10 mm, C = 18 mm, L = 128 mm, and R = 0.2 mm.

III. RESULTS

Using the design dimensions determined in the previous section, the antenna was built and measured as well as simulated using three different computational electromagnetic software, namely: FEKO, Ansys HFSS, and CEMS. For comparison purposes a dipole antenna with the same length as the modified dipole antenna design is also simulated and tested. Figure 5 shows the magnitude of S_{11} versus frequency for the dipole antenna modeled in FEKO and the modified dipole configuration in the three different software packages.

Table 1 shows the original bandwidth and the corresponding improvement for each dipole simulation. The center frequency was determined by finding the -10 dB crossings and calculating the frequency in the middle. For the three modified dipole antennas results in

Fig. 5, the curves are different regions below -10 dB but exhibit a similar behavior. The slight differences can be due to the nature of the three different software packages and how they represent the antenna and the source of excitation. All of the modified dipole models operate at a higher frequency than the traditional dipole antenna and the reflection coefficient curves have two local minimums. The mean improvement in bandwidth is more than four times when comparted to the traditional dipole antennas as can be seen in Table 1. Figure 6 shows the measured reflection coefficient for the two models shown in Fig. 1. The curve does not closely resemble what was simulated, but the overall result is similar. The difference is due to the un-professional construction of the antenna, SMA connector, and from the solder joints which was not accounted for in simulations. The bandwidth of the fabricated modified dipole was improved by approximately four times when compared to the fabricated dipole antenna.

To study the effect of the additional wire elements FEKO was used to examine the radiated far-field patterns. The electric field was examined for the modified dipole antenna as well as a dipole antenna operating at the center frequency of the modified dipole antenna.

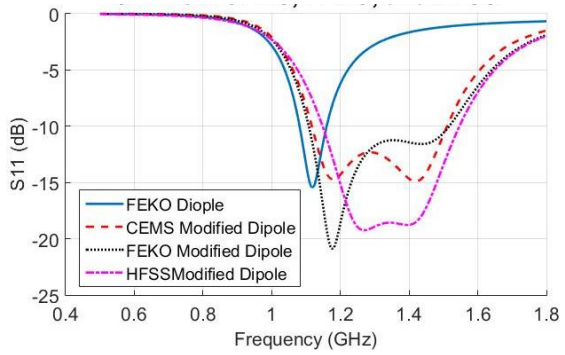

Fig. 5. Reflection coefficient for a regular dipole and the modified dipole using three different software packages.

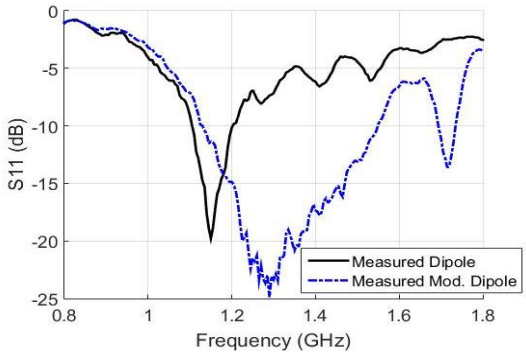

Fig. 6. Measured reflection coefficient for a regular dipole and the modified dipole.

Table 1: Bandwidths of the dipole antennas

Antenna	BW (%)	% BW Improvement
FEKO dipole	7.05	-
CEMS mod. dipole	30.37	23.32
FEKO mod. dipole	31.17	24.12
HFSS mod. dipole	30.35	25.36
Measured dipole	8.24	-
Measured mod. dipole	31.78	23.54

From Figs. 7 and 8 it is observed that the addition of the wire elements does not drastically change the magnitude of E_θ in all three planes across the frequency band. Table 2 shows the gain for both the modified antenna and dipole antenna at three different frequencies within the band.

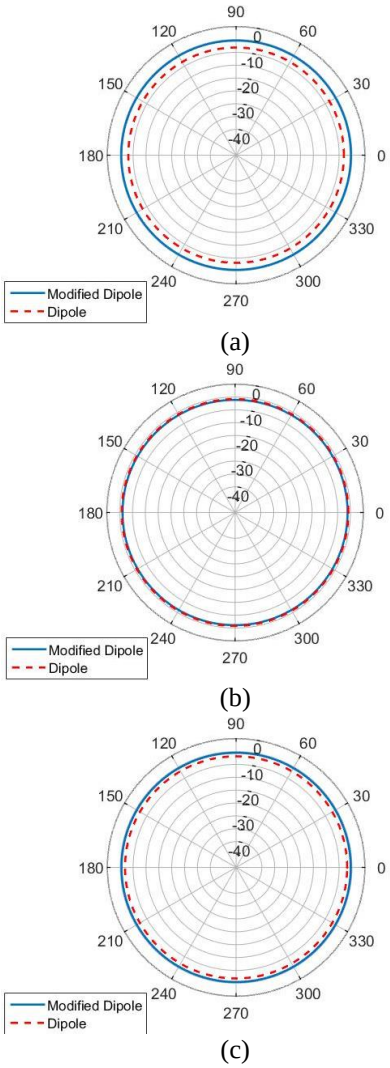

Fig. 7. Electric field in the XY-plane: (a) 1.202 GHz, (b) 1.306 GHz, and (c) 1.410 GHz.

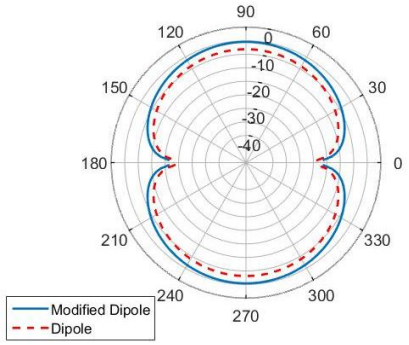

(a)

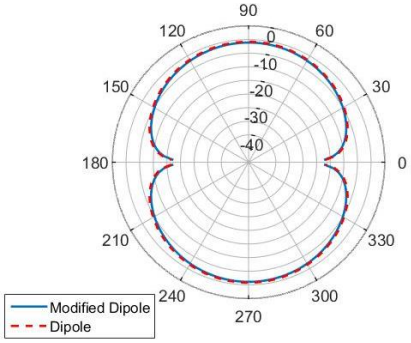

(b)

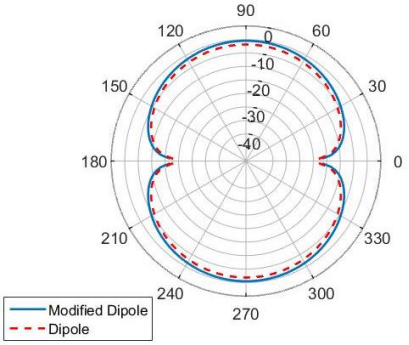

(c)

Fig. 8. Electric field in the XZ-plane and YZ-plane: (a) 1.202 GHz, (b) 1.306 GHz, and (c) 1.410 GHz.

Table 2: Realized gain of modified dipole using FEKO

	Realized Gain (dBi)		
Antenna	1.202 GHz	1.31 GHz	1.41 GHz
Modified dipole	2.117	1.92	1.92

Due to the better matching at the input port of the modified dipole, the realized gain of the modified antenna remains around 2 dBi for all three frequencies. The calculated gain of the traditional dipole antenna is 1.94 dBi.

VI. CONCLUSION

A modified dipole antenna configuration is proposed and investigated using three different software packages as well as measured results from built antennas. Additional wire elements are added to a traditional half wave length antenna that enable impedance matching across the band. It is shown numerically and experimentally that this configuration can increase the input impedance bandwidth four times when compared to a traditional dipole antenna. The additional wires do not change the radiation characteristics of the dipole antenna as demonstrated using simulations. The resulting cross polarized electric field component E_ϕ is found to be less than 40 dB of the E_θ component. The gain of the modified antenna is close to 2 dBi over a broad range of frequencies. Based on this study, the proposed modified dipole antenna has the potential to expand the use of dipole antennas in a wide range of applications.

REFERENCES

[1] H.-T. Hsu, J. Rautio, and S.-W. Chang, "Novel planar wideband omni-directional quasi logperiodic antenna," *Asia Pacific Microwave Conference (APMC)*, Suzhou, China, Dec. 2005.

[2] A. Z. Elsherbeni, P. Nayeri, and C.J. Reddy, *Wire Dipole and Monopole Antennas*, in Antenna Analysis and Design Using FEKO Electromagnetic Simulation Software, ACES Series on Computational Electromagnetics and Engineering, SciTech Publishing, an Imprint of IET, Edison, NJ, pp. 36-38, 2014.

[3] G. R. Hoch, P. Nayeri, and A. Z. Elsherbeni, "Bandwidth enhancement of dipole antennas using parasitic elements," *The 31st International Review of Progress in Applied Computational Electromagnetics (ACES 2015)*, 2015.

[4] FEKO, EM Software & Systems Inc., Version 7.0.2. https://www.feko.info/

[5] HFSS, Ansys, Release 16.2.0. http://www.ansys.com

[6] CEMS, EM software package based on A. Elsherbeni and V. Demir, *The Finite-Difference Time-Domain Method for Electromagnetics with Matlab Simulations*, ACES Series on Computational Electromagnetics and Engineering, 2nd Edition, SciTech Publishing, an Imprint from IET, Edison, NJ, 2016.

CUDA-MPI Implementation of Fast Multipole Method on GPU Clusters for Dielectric Objects

Nghia Tran, Tuan Phan, and Ozlem Kilic

Department of Electrical Engineering and Computer Science
The Catholic University of America, Washington, DC, 20064, USA
16tran@cua.edu, 30phan@cua.edu, kilic@cua.edu

Abstract ─This paper investigates the Fast Multipole Method (FMM) for large-scale electromagnetics scattering problems for dielectric objects. The algorithm is implemented on a Graphical Processing Unit (GPU) cluster using CUDA programming and Message Passing Interface (MPI). Its performance is investigated in terms of accuracy, speedup, and scalability. The details of the implementation and the performance achievements are shown and analyzed, demonstrating a scalable parallelization while maintaining a good degree of accuracy.

Index Terms ─ Dielectric objects, Fast Multipole Method (FMM), Graphics Processing Unit (GPU), Message Passing Interface (MPI).

I. INTRODUCTION

Modelling electrically large dielectric objects plays an important role in the research of target identification or the stealth and anti-stealth technology. The excessively heavy requirements of memory and computational resources of such applications pose a challenging problem in the computational electromagnetics community. The past two decades have witnessed many numerical techniques developed to reduce this burden without significant loss of accuracy, including Adaptive Integral Method (AIM) [1], Impedance Matrix Localization (IML) [2], and Fast Multipole Method (FMM) [3]. Among others, FMM is the most suitable technique for large-scale problems in reducing the computational complexity of the conventional technique, Method of Moment (MoM) [4] from $O(N^3)$ to $O(N^{1.5})$, where N denotes the number of unknowns. Some other approaches such as AIM and IML have the complexity of $O(N^{1.5}logN)$ and $O(N^2logN)$, respectively. Many authors have investigated the parallelization of FMM on CPU clusters for solving the dielectric problems [5]. However, to the best of our knowledge, FMM has not been studied for dielectric electromagnetics problems on GPU clusters. Recently our group has applied single-level FMM for perfect electric conductor (PEC) objects [6]-[7], and good speedup factors compared to the CPU implementations were achieved. However, our previous implementations focused only on PEC objects, which can be limiting for simulating real-life scenarios.

In this paper, we investigate the parallelization of FMM for dielectric electromagnetics structures using the PMCHW formula [8] on a multi-node GPU cluster with CUDA and MPI programing. We demonstrate that the implementation of FMM on GPU clusters outperforms that of the CPU counterpart in terms of speedup and scalability.

The rest of the paper is organized such that Section II provides an overview of FMM for dielectric objects. Section III describes the parallelization of FMM on GPU clusters. Experimental results are discussed in Section IV. Finally, our findings are summarized in the conclusions section.

II. OVERVIEW OF THE FAST MULTIPOLE METHOD FOR DIELECTRIC OBJECTS

In this section, we provide a brief overview to help our discussion on the parallel implementation of FMM for dielectric objects, which is presented in detail in Section III.

FMM solves for the linear equation system created in the form of $ZI = V$, where I represents the unknown currents, V depends on the incident field, and Z is the impedance matrix. The main idea of FMM is the grouping concept as shown in Fig. 1, where N edges in the mesh of a given structure are categorized into M localized groups based on their proximity. According to this approach, two interaction types can be defined: near and far, as depicted in Fig. 1. The Z matrix is split into two components, Z^{near} and Z^{far}, as shown in (1):

$$\sum_{m'}^{M} Z_{mm'} I_{m'} = \sum_{m'}^{M} Z_{mm'}^{near} I_{m'} + \sum_{m'}^{M} Z_{mm'}^{far} I_{m'} = V_m,$$
$$\text{where } Z_{mm'} = \begin{bmatrix} Z_{mm',JJ} & Z_{mm',JM} \\ Z_{mm',MJ} & Z_{mm',MM} \end{bmatrix}, V_m = \begin{bmatrix} E_m \\ H_m \end{bmatrix}, \quad (1)$$

and m and m' are observation and source edges in the mesh, respectively.

The near term comprises of interactions between

Submitted On: July 14, 2016
Accepted On: August 17, 2016

spatially close edges, and is computed and stored in a similar manner to MoM [4]. For dielectric objects, PMCHW formula [8] is used in this paper and the four components of Z^{near} is shown in (2)-(4):

$$Z^{near}_{mm',JJ} = \frac{j\omega\mu}{4\pi}\int_S \boldsymbol{f}_{m'}(\boldsymbol{r}')\int_S G_1(\boldsymbol{r},\boldsymbol{r}')\bullet \boldsymbol{f}_m(\boldsymbol{r})dS'dS + \frac{1}{4\pi\, j\omega\varepsilon}\int_S(\nabla\bullet \boldsymbol{f}_m(\boldsymbol{r}))\int_S G_1(\boldsymbol{r},\boldsymbol{r}')\bullet(\nabla\bullet \boldsymbol{f}_{m'}(\boldsymbol{r}'))dS'dS, \quad (2)$$

$$Z^{near}_{mm',MM} = \frac{j\omega\varepsilon\eta^2}{4\pi}\int_S \boldsymbol{f}_{m'}(\boldsymbol{r}')\int_S G_1(\boldsymbol{r},\boldsymbol{r}')\bullet \boldsymbol{f}_m(\boldsymbol{r})dS'dS + \frac{\eta^2}{4\pi\, j\omega\mu}\int_S(\nabla\bullet \boldsymbol{f}_m(\boldsymbol{r}))\int_S G_1(\boldsymbol{r},\boldsymbol{r}')\bullet(\nabla\bullet \boldsymbol{f}_{m'}(\boldsymbol{r}'))dS'dS, \quad (3)$$

$$Z^{near}_{mm',MJ} = \frac{-\eta}{4\pi}\int_S \boldsymbol{f}_{m'}(\boldsymbol{r}')\int_S \nabla G_1(\boldsymbol{r},\boldsymbol{r}')\times \boldsymbol{f}_m(\boldsymbol{r})dS'dS = -Z^{near}_{mm',JM}. \quad (4)$$

The interactions between the remaining edges that are spatially far from each other constitute the far term. The advantage of separating the Z matrix into two components is that the Z^{far} matrix does not need to be computed and stored ahead of time. Instead it is factorized into the radiation, T^E/T^{ED}, receive, R^E, and translation functions, T_L. Equations (5)-(11) depict these functions based on PMCHW formula:

$$Z^{far}_{mm',JJ} = \frac{\omega\mu k}{16\pi^2}\int d^2\hat{\boldsymbol{k}}\, \boldsymbol{T}^E_{r_{im}}(\hat{\boldsymbol{k}})T_L(k,\hat{\boldsymbol{k}},\boldsymbol{r}_{ii'})\bullet R^E_{m'i'}(\hat{\boldsymbol{k}}), \quad (5)$$

$$Z^{far}_{mm',MM} = \frac{\omega\varepsilon k\eta^2}{16\pi^2}\int d^2\hat{\boldsymbol{k}}\, \boldsymbol{T}^E_{r_{im}}(\hat{\boldsymbol{k}})T_L(k,\hat{\boldsymbol{k}},\boldsymbol{r}_{ii'})\bullet R^E_{m'i'}(\hat{\boldsymbol{k}}), \quad (6)$$

$$Z^{far}_{mm',MJ} = \frac{k\eta}{16\pi^2}\int d^2\hat{\boldsymbol{k}}\, \boldsymbol{T}^{ED}_{r_{im}}{}'(\hat{\boldsymbol{k}})T_L(k,\hat{\boldsymbol{k}},\boldsymbol{r}_{ii'})\bullet R^E_{m'i'}(\hat{\boldsymbol{k}}) = -Z^{far}_{mm',JM}, \quad (7)$$

where

$$T^E_{r_{im}} = \int_S (\boldsymbol{I} - \hat{\boldsymbol{k}}\hat{\boldsymbol{k}})\bullet \boldsymbol{f}_m(\boldsymbol{r}_{im})e^{-j\boldsymbol{k}\bullet\boldsymbol{r}_{im}}dS, \quad (8)$$

$$T^{ED}_{r_{im}} = \int_S \hat{\boldsymbol{k}}\times \boldsymbol{f}_m(\boldsymbol{r}_{im})e^{-j\boldsymbol{k}\bullet\boldsymbol{r}_{im}}dS, \quad (9)$$

$$R^E_{r_{m'i'}} = \int_S \boldsymbol{f}_{m'}(\boldsymbol{r}_{m'i'})e^{-j\boldsymbol{k}\bullet\boldsymbol{r}_{m'i'}}dS, \quad (10)$$

$$T_L = \sum_{l=0}^{L}(-j)^l(2l+1)h_l^{(2)}(\boldsymbol{k}\bullet\boldsymbol{r}_{ii'})P_l(\hat{\boldsymbol{k}}\bullet\boldsymbol{r}_{ii'}). \quad (11)$$

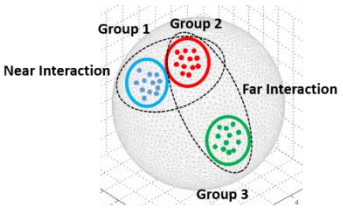

Fig. 1. FMM grouping concept.

In the equations above, the prime syntax denotes the source points, and i refers to the groups in the mesh. The unit vector $\hat{\boldsymbol{k}}$ denotes the K possible field directions in k space, $\boldsymbol{f}(\mathbf{r})$ denotes the basic functions, $h_l^2(r)$ is the spherical Hankel function of the second kind, and $P_l(r)$ is the Legendre polynomial.

III. PARALLELIZATION OF FMM ON GPU CLUSTERS

The platform utilized in our FMM implementation is a GPU cluster, which consists of 13 computing nodes. Each node has a dual 6-core 2.66 GHz Intel Xeon processor, 48 GB RAM along with one NVidia Tesla M2090 GPU running at 1.3 GHz with 6 GB memory. The nodes are interconnected through the infiniBand interconnection. The cluster populates CUDA v7.0 and MVAPICH2 v1.8.1. (a well-known implementation of Message Passing Interface (MPI)). Two parallel programming approaches of CUDA and MPI are combined to provide the use of GPU programming across the cluster.

In this section, we provide an overview of our implementation on GPU. Figure 2 shows the main blocks which consist of pre-processing, processing and post-processing, where processes which utilize GPU are shown in solid green line, and CPU based operations are shown in dashed black line. The geometry mesh data resulting from the pre-processing step is transferred to the GPU memory, and the entire computation is performed on the GPU. The user defined results such as radar cross section, scattered fields are post-processed on the CPU.

The parallelization of the processing step in GPU cluster implementation is performed at two levels: (i) among computing nodes using MPI library, and (ii) within GPU per node using CUDA programming model. The workload of the computational task is equally distributed among the computing nodes, and the inter-node communication is minimized. This is achieved by uniformly distributing the total number of groups, M, among the n computing nodes. We only present the far interactions in this paper, since the near field and V vector calculations implementations can be found in [6]-[7].

A. Far interactions calculations

This task comprises of three calculations: radiation, and receive functions and translation matrices. The first step in the far interaction calculations is the calculation of the radiation, T^E/T^{ED} and receive, R^E, functions for Z^{far} matrix as seen in Fig. 2. It is worth noting that the radiation and the receive functions as well as the translation matrix have to be evaluated at all K directions for the unit sphere integration. The computational workload is distributed across the nodes using the group-based partitioning scheme such that M_{node} groups are allocated for each node. K evaluations for the radiation and receive functions are required for each node. The threads are grouped into blocks such that each block of threads performs N_{group} radiation/receive functions at a given group, then a total number of blocks per node

equal to $M_{node}K$.

The second task for far interactions is the calculation of the translation matrix, T_L. Similar to the calculation of the radiation/receive functions, the translation matrix has to be evaluated at all K directions for the unit sphere integration. The workload for the T_L calculations is also distributed across the nodes following the group-based technique. Each CUDA block is assigned to compute one sparse row of the T_L matrix for a given direction, and each thread computes one element in that row.

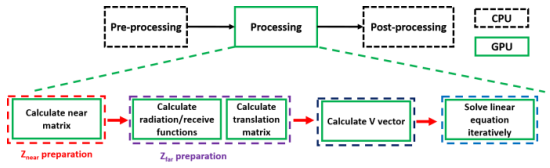

Fig. 2. FMM flow chart implementation.

B. Fast matrix-vector multiplication

The processing step is followed by solving linear equation iteratively. In this paper, the Biconjugate Gradient Stabilized method (BICGSTAB) is employed where each iteration involves the Matrix-Vector Multiplication (MVM). In this part, MVM of the far interactions are focused and the calculation of $Z_{far}I$ comprises of aggregation, translation, and disaggregation. By using the group-based scheme, the inter-node communication is required only at two steps: (i) at the beginning of the MVM to exchange the estimated values for the unknowns among the nodes, and (ii) after the aggregation step and before performing the translation step in order to update all nodes with the aggregated fields. The flow chart of the implementation is shown in Fig. 3.

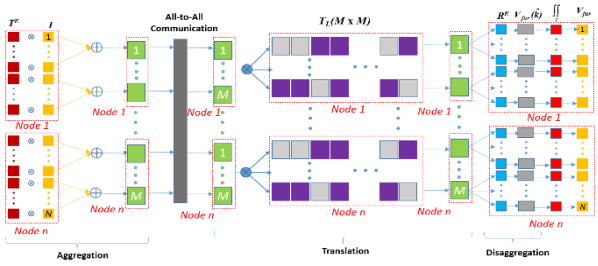

Fig. 3. Far-interaction flow chart implementation.

Each node already calculates its own portion of the radiation/receive functions, and the translation matrix. In the aggregation stage, each unknown is multiplied with its corresponding radiation functions, and is summed in each group. The aggregation stage can be performed independently for all K directions, and thus can be performed concurrently with minimal need for inter-node communication. An all-to-all communication is employed by each node to broadcast the aggregated fields to all other nodes. Then the received fields at each direction are determined by multiplying the aggregated fields with the translation matrix. Next the received fields are multiplied with the receive functions to obtain the field for each group at a given direction. Finally, an integration over the K directions of the unit sphere is performed to calculate the fields at each observed edge. The far MVM is incorporated with the near MVM to get the full ZI.

IV. EXPERIMENTAL RESULTS

A. Accuracy

To validate the accuracy of FMM implementations on GPU clusters, we calculate the radar cross section (RCS) of a 14λ diameter (254,274 unknowns) sphere with permittivity ε = 4 – 0.1j. It is illuminated by a normally incident 1 GHz x-polarized plane wave. The RCS based on our GPU implementation is compared to the results of the analytical Mie scattering. Figure 4 shows that the GPU and Mie solutions achieve a good agreement.

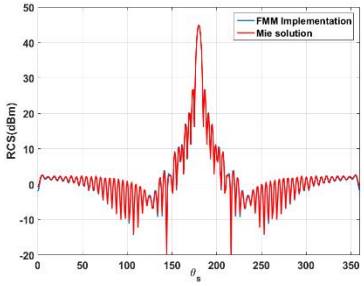

Fig. 4. RCS of a 14λ diameter dielectric sphere

B. Implementation performance on GPU cluster

Our GPU implementations is evaluated using the fixed-workload model in the first experiment. We choose a sphere diameter of 12.4λ, ~ 200K unknowns for the fixed problem size such that it demands the use of at least 8 nodes to satisfy the required memory. Speedup and scalability are used to evaluate the GPU implementations. The speed up is defined as the ratio of time required by multi-node GPU implementation with respect to the 8-node CPU implementation. Scalability is the normalized speedup of multiple nodes in reference to the speedup of 8 nodes. In our analysis, we consider the total executional time and computational time. Figure 5 shows the speedup factors and the measured time of two cases. It is observed that the computation time achieves a speedup factor of 171.5 on 8 nodes, and takes 158.9 seconds. Due to the nature of the fixed workload model, each node carries less workload when the number of computing nodes increase. Therefore the computation time decreases linearly with the increase in nodes (274.5 seconds for computation and 229.9 seconds for total). The slightly smaller speedup factors for the total time as compared to the computation time are due to the inter-node

communications for transferring the data in our GPU implementations.

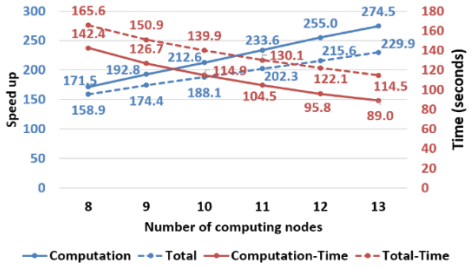

Fig. 5. Speedup analysis for the fixed-workload model (vs. 8 nodes CPU implementation, 100 iterations) Computational CPU exec time = 24,421 sec, total CPU exec time = 26,315 sec.

It is observed in Fig. 6 that both computation and total time scale closely to the theoretical linear expectation for the fixed workload problem. This good scalability demonstrates that our implementation has efficiently parallelized the algorithm and reduced the communication overhead.

The second experiment is the fixed-time model. As the problem size is increased, the number of nodes also increases, so that the GPU memory in each node is fully utilized. Our GPU implementation can process a maximum problem size of 254K unknowns with a speedup factor of 169.6 for the computation, and 137 for total execution time as shown in Fig. 7.

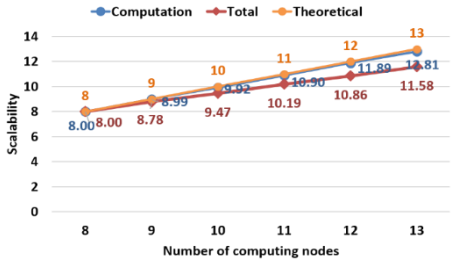

Fig. 6. Scalability analysis for the fixed-workload model.

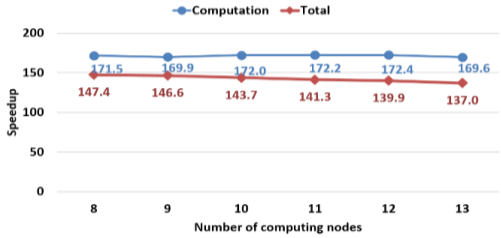

Nodes	8	9	10	11	12	13
Size (Diameter/ unknowns)	12.4λ/ 199K	12.7λ/ 209K	13.1λ/ 222K	13.5λ/ 234K	13.8λ/ 246K	14λ/ 254K

Fig. 7. Speedup analysis when the number of nodes increases along with problem size increases (vs. multi-node CPU, 100 iterations).

VI. CONCLUSION

In this paper, the GPU implementation of FMM for dielectric electromagnetic scattering problems using our 13-node GPU cluster is demonstrated. The maximum problem size is determined by the available on-board GPU memory. For the same degree of accuracy, the GPU implementation outperforms the CPU implementation. Moreover, the GPU implementation has a good scalability as the number of computing nodes increases.

REFERENCES

[1] E. Bleszynski, M. Bleszynski, and T. Jaroszewicz, "AIM: Adaptive integral method for solving large-scale electromagnetic scattering and radiation problems," *Radio Science*, vol. 31, no. 5, pp. 1225-1251, 1996.

[2] F. X. Canning, "The impedance matrix localization (IML) method for moment-method calculations," *IEEE Antennas Propagat. Mag.*, vol. 32, no. 5, pp. 18-30, 1990.

[3] R. Coifman, V. Rokhlin, and S. Wandzura, "The fast multipole method for the wave equation: A pedestrian prescription," *IEEE Antennas Propagat. Mag.*, vol. 35, no. 3, pp. 7-12, June 1993.

[4] S. M. Rao, D. R. Wilton, and A. W. Glisson, "Electromagnetic scattering by surfaces of arbitrary shape," *IEEE Trans. Antennas Propag.*, vol. AP-30, no. 3. pp. 409-418, May 1982.

[5] O. Ergul and L. Gurel, "Efficient parallelization of the multilevel fast multipole algorithm for the solution of large-scale scattering problems," *IEEE Trans. Antennas Propag.*, vol. 56, no. 8, pp. 2335-2345, August 2008.

[6] Q. M. Nguyen, V. Dang, O. Kilic, and E. El-Araby, "Parallelizing fast multipole method for large-scale electromagnetic problems using GPU clusters," *Antennas and Wireless Propagation Letters, IEEE*, vol. 12, pp. 868-871, 2013.

[7] V. Dang, Q. Nguyen, and O. Kilic, "Fast multipole method for large-scale electromagnetic scattering problems on GPU cluster and FPGA-accelerated platforms," *Applied Computational Electromagnetics Society Journal*, vol. 28, no. 12, 2013.

[8] X. Q. Sheng, J.-M. Jin, J. Song, W. C. Chew, and C.-C. Lu, "Solution of combined-field integral equation using multilevel fast multipole algorithm for scattering by homogeneous bodies," *IEEE Transactions on Antennas and Propagation*, vol. 46, no. 11, pp. 1718-1726, 1998.

Vector Control of PMSM Take Over by Photovoltaic Source

T. Yuvaraja [1] and K. Ramya [2]

[1] Department of Electrical and Electronics Engineering
Sri Sairam College of Engineering, Bangalore City, Karnataka - 632001, India
yuvarajastr@gmail.com

[2] Department of Electrical and Electronics Engineering
Sri Sairam College of Engineering, Bangalore City, Karnataka - 632001, India
ramyaj.k14@gmail.com

Abstract — This article established with the modeling and the field oriented control of permanent magnet synchronous machines, with a focus on their applications in variable speed domain in photovoltaic source.

Index Terms — Field oriented control, inverter, permanent magnet synchronous machine, photovoltaic.

I. INTRODUCTION

The permanent magnet synchronous motor (PMSM) has three phases winding on stator represented by the three axes (a, b, c) phase-shifted of 120° with respect to each other (Fig. 1) and has permanent magnets in the rotor ensuring its excitation. Depending on how the magnets are placed, we can distinguish two types of rotors; in the first type, the magnets are mounted on the surface of the rotor with a homogeneous air gap, the motor is called "smooth air gap PMSM" and inductors are independent on the rotor position. In the second type, the magnets are mounted inside the rotor mass and the air gap will vary because of the salience effect. In this case, inductors are highly dependent on the rotor position. Synchronous motors have a remarkable feature; the speed is constant regardless of the load. The field oriented control (FOC) is used for many years. It implements Park transformation which shows, like a separately excited dc machine, the expression of the instantaneous torque as a product of magnetic flux and current. In addition, there is the possibility to reduce the oscillations for a desired torque, to save energy delivered, to reduce the current harmonics and to improve power factor. When the motor model used is correct, the FOC works well [1-6].

II. DYNAMIC MODEL OF SYNCHRONOUS MOTOR

A. Mathematical model of PMSM

The dynamic model of a permanent magnet synchronous motor with rotor reference frame can be described by the equations below, considering the conditions of non-saturation of the magnetic circuit and the magneto motive force MMF is a sinusoidal distribution created by the stator windings:

$$[V_{abc}] = [RI_{abc}] + \frac{d(\varphi_{abc})}{dt}, \tag{1}$$

$$[V_{abc}] = \begin{bmatrix} V_a \\ V_b \\ V_c \end{bmatrix}; [i_{abc}] = \begin{bmatrix} i_a \\ i_b \\ i_c \end{bmatrix}; [\varphi_{abc}] = \begin{bmatrix} \varphi_a \\ \varphi_b \\ \varphi_c \end{bmatrix} [R] = \begin{bmatrix} R & 0 & 0 \\ 0 & R & 0 \\ 0 & 0 & R \end{bmatrix}, \tag{2}$$

with $V_{abc}, i_{abc}, \phi_{abc}$ representing the stator phases' voltages, the stator phases' currents and the total flux produced by the stator currents. R indicates the resistance of a stator phase.

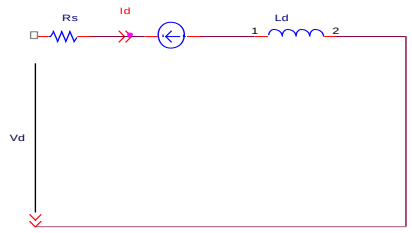

Fig. 1. Equivalent circuit of a permanent magnet synchronous motor in the dq frame.

Total fluxes are expressed by:

$$(\varphi_{abc}) = (L)(i_{abc}) + (\varphi'_{abc})$$

$$L = \begin{bmatrix} L_{ss} & M_s & M_s \\ M_s & L_{ss} & M_s \\ M_s & M_s & L_{ss} \end{bmatrix}, \tag{3}$$

L_{ss} and M_s representing the self-inductance and the mutual inductance between stator windings. ϕ'_{abc} is the rotor flux seen by the stator windings. It represents the amplitudes of the voltages induced in the stator phases without load. Substituting (3) in (1):

Submitted On: July 27, 2016
Accepted On: August 16, 2016

$$[V_{abc}] = (R)(i_{abc}) + L\frac{d(i_{abc})}{dt} + \varphi'_{abc}. \quad (4)$$

The electromagnetic torque is expressed by:

$$T_e = \frac{1}{\omega_r}(e_{abc})^t(i_{abc}), \quad (5)$$

where $e_{abc} = \frac{d(\phi_{abc})}{dt}$ represents the electromotive forces generated by the stator phases. ω_r is rotation speed of the rotor in [rad/s]. Note that the system (4) leads to joined and highly non-linear equations. To simplify this problem, the majority of research in literature prefer to use the Park transformation which, by a transformation applied to real variables (voltages, currents and flux), provides fictive variables called dq components of Park's equations. Physically, this transformation is interpreted as a substitution for stationary windings (a,b,c) by rotating windings (d,q) which rotate with the rotor. This transformation makes the dynamic equations of AC motors simpler. The Park transformation is defined as follows:

$$(x_{dq0}) = (K_\theta)(x_{abc}), \quad (6)$$

where X may be a current, a voltage or a flux and θ is the rotor position. X_{dq} represent longitudinal and transversal components of the stator variables (voltages, currents, fluxes and inductances). The transformation matrix K_θ is by:

$$[K_\theta] = \sqrt{\frac{2}{3}}\begin{bmatrix} \frac{1}{\sqrt{2}} & Cos\theta & -Sin\theta \\ \frac{1}{\sqrt{2}} & Cos\left(\theta - \frac{2\pi}{3}\right) & -Sin\left(\theta - \frac{2\pi}{3}\right) \\ \frac{1}{\sqrt{2}} & Cos\left(\theta - \frac{4\pi}{3}\right) & -Sin\left(\theta - \frac{4\pi}{3}\right) \end{bmatrix}. \quad (7)$$

The inverse matrix:

$$[K_\theta]^{-1} = [K_\theta]^t = \begin{bmatrix} \frac{1}{\sqrt{2}} & \frac{1}{\sqrt{2}} & \frac{1}{\sqrt{2}} \\ Cos\theta & Cos\left(\theta - \frac{2\pi}{3}\right) & Cos\left(\theta - \frac{4\pi}{3}\right) \\ -Sin\theta & -Sin\left(\theta - \frac{2\pi}{3}\right) & -Sin\left(\theta - \frac{4\pi}{3}\right) \end{bmatrix}. \quad (8)$$

Applying the transformation (6) to the system (1), we have the electrical equations in the d_q reference:

$$[V_d] = [R_s I_{sd}] + \frac{d(\varphi_{sd})}{dt} - \omega_r \varphi_{sq}, \quad (9)$$

$$[V_q] = [R_s I_{sq}] + \frac{d(\varphi_{sq})}{dt} - \omega_r \varphi_{sd}. \quad (10)$$

The flux equation:

$$\varphi_{sd} = L_{sd} i_{sd} + \varphi_f, \quad (11)$$

$$\varphi_{sq} = L_{sq} i_{sq}, \quad (12)$$

ϕ_f is the flux created by the magnets in the rotor. By replacing (11) and (12) and in $v_{q,} v_d$ we obtain the following equations:

$$V_d = R_s i_{sd} + L_{sd}\frac{di_{sd}}{dt} - \omega_r L_{sq} i_{sq}, \quad (13)$$

$$V_q = R_s i_{sq} + L_{sq}\frac{di_{sq}}{dt} + \omega_r\left(L_{sd} i_{sd} + \varphi_f\right). \quad (14)$$

Equations (13) and (14) form a second order differential equation system that models the electrical behaviour of the synchronous permanent magnet [1], [2].

III. FIELD ORIENTED CONTROL

We can determine the reference torque to impose on the motor and the speed reference from the electromagnetic torque equation expressed in terms of Park's components, if we impose the current. To preserve the torque *Te* proportional to the current *isq*, we must control the angle α = π/2, and the angle α is determined by the following formula.

A. Inverter modeling

The inverter transforms a DC voltage into an alternating voltage with a varying amplitude and frequency. Its bridge structure is composed mostly of electronic switches such as IGBTs, power transistors or thyristors. Its operating principle is based on controlled switching in a suitable manner (usually a pulse width modulation), the source is modulated to obtain a wanted AC signal frequency. Two types of inverters are used; the voltage inverter and the current inverter. The voltage inverter with six switches, supplied by the photovoltaic generator and operating in pulse-width modulation (PWM) is commonly used for this application in Fig. 2.

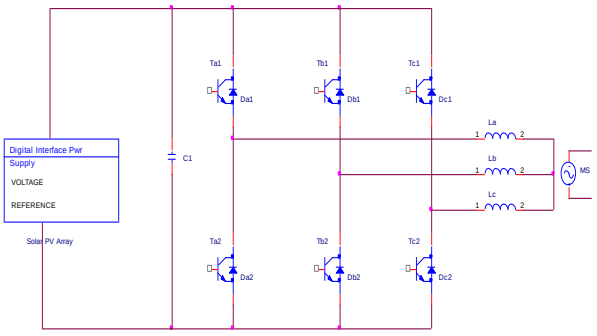

Fig. 2. PMSM supply using voltage inverter.

B. The hysteresis current control technique

It is a simple technique directly interested in current control; it limits the maximum current and is less sensitive to load variations. This method is used to control the current of a to follow a sinusoidal reference current calculated from the currents i_{sdref}, i_{sqref} and from the rotor position ϕ. If the error, which is the difference between the reference current of a phase and the same phase current reached the upper limit $(i_{ref} + \Delta I)$, the switch

arm of the inverter corresponding to the same phase is started and connected to the (-) pole of the power source to reduce the current; while if the error reached the lower limit $(i_{ref} - \Delta I)$, the switch connected to the positive terminal of the power source should be started to increase the flow of the corresponding phase. The lower and upper limits of the hysteresis band ΔI are set by the motor absorbed current and the maximum switching frequency of switches respectively. A narrow band of hysteresis implies a current more similar to the sine wave with a low harmonic content, and a switching frequency higher and higher, and vice versa.

The current references are given by voltage inverter in such to force the phase currents of the motor these currents are sinusoidal functions of rotor position. They create in the gap a field with magnetic axis in quadrature with the axis of the magnets' field. They are in phase with the electromotive forces induced in these windings by the magnets. When the reference current in a phase deviates from its reference, each controller requires switching the switches of each inverter arm and keeps it within the hysteresis band ΔI in Fig. 3.

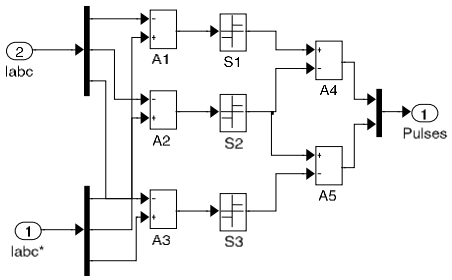

Fig. 3. Representation of hysteresis current control.

C. Modeling of the photovoltaic cell

The photovoltaic generator which produces a continuous electrical current is represented by a standard model with a single diode, established by Shockley for a single PV cell and generalized to a PV module by considering it as a set of identical cells connected in series-parallel [4].

IV. SPEED CONTROLLER DESIGN

The design of the speed controller is important from the point of view of imparting desired transient and steady state characteristics to speed controlled PMSM drive system. A proportional pulse integral controller is sufficient for many industrial applications. Selection of the gain and time constant of such a controller by using the symmetric optimum principle is straightforward if the d axis stator current is assumed to be zero in Fig. 4.

In the presence of a d axis stator current, the d and q current channels are cross couples, and the model is nonlinear, as a result of the torque term [5], [6]. A proportional plus integral (PI) controller is used to process the speed error between the speed reference and filtered speed feedback signals, the transfer function of the speed controller is given as in Fig. 5.

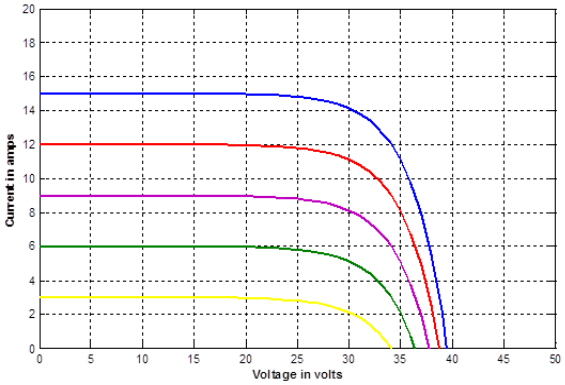

Fig. 4. Characteristics of the power function of the current and the voltage.

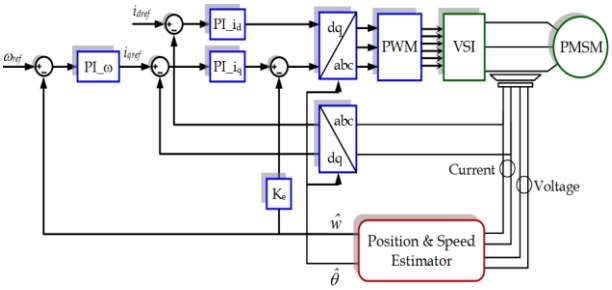

Fig. 5. Block diagram of a speed controlled PMSM drive.

A. Current loop

This induced emf loop crosses the q axis current loop, and it could be simplified by moving the pick-off point for the induced emf loop from speed to current output point. This gives the current loop transfer function in Fig. 6.

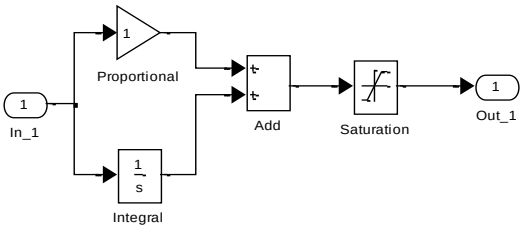

Fig. 6. Implantation the speed controller with saturation in Simulink.

V. LOAD TESTING WITH CONSTANT RESISTANCE TORQUE

The system established in Simulink for a drive system of PMSM with reference current hysteresis control method.

Figures 7-8 shows phase currents of the synchronous motor with permanent magnet. It is clear that the currents are not sinusoidal at startup and becomes sinusoidal when the motor reaches the steady state. The motor absorbs a high current at start-up. i_{dq} currents increase when the motor is controlled by oriented flux, the current i_d is zero ($i_d = 0$), while i_q current increases at start up then stabilizes in steady state. The torque *Te* developed by the motor follows the instructions properly; its value at startup is five times the value of the rated torque.

Steady speed is the same as that of the commanded speed reference (1790 tr/mn). Simulink program of Matlab is used for simulation tests The PMSM parameters used in the tests are as follows: stator Resistance Rs = 1.4 Ω, stator inductance $L_d = L_q = 0.0006$ Henry Magnet flux linkage $\varphi_f = 0.1679$ *Tesla*/m^2 System inertia J = 0.01176 kgm^2, viscous friction coefficient B = 0.00338818 N.s/rad, DC link voltage using the Lookup Table block in Simulink. We insert the values of the voltage at the PV generator. rated electrical speed ω_n = 1850 tr/mn, pole pairs np = 3 The phase voltages are reconstructed from DC-bus voltage and duty cycle; motor currents are filtered by a three-order low pass filter with pass band edge frequency equal to 12666 rad/s.

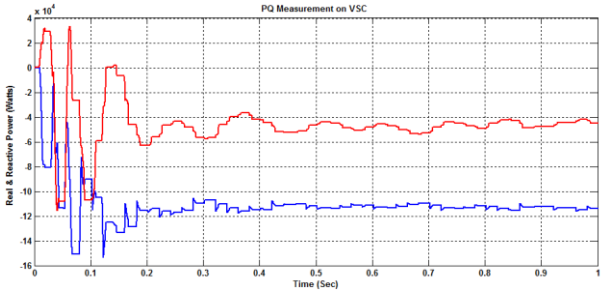

Fig. 7. Diagram of I_{abc} versus time.

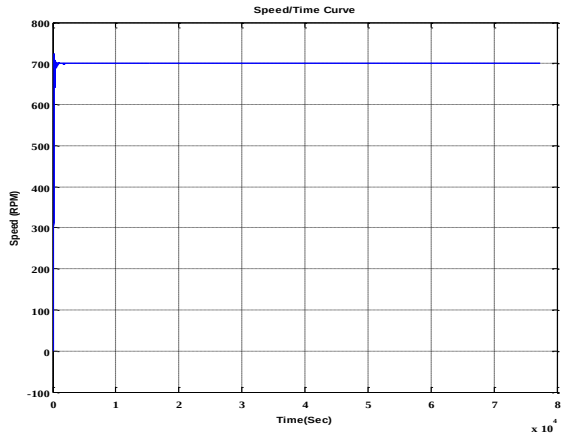

Fig. 8. Diagram of speed versus time.

VI. CONCLUSION

The vector control is introduced in order to control the permanent magnet synchronous machine with maximum power. It is based on a transient model. It allows precise adjustment of the torque of the machine and can ensure torque at zero speed. In this paper, we have presented the principle of the permanent magnet synchronous motor field oriented control, fed by a voltage inverter in the presence of a speed loop with a PI corrector. We can conclude that the field oriented control has a good dynamic and static torque and flux results. View that the radiation and temperature are variable in the day it would be interesting in future work to introduce a buck or boost chopper between the PV generator and the inverter to extract maximum energy delivered by the photovoltaic generator.

REFERENCES

[1] A. Kaddouri, "Étude d'une Commande Non-Linéaire Adaptative d'une Machine Synchrone À Aimants Permanents," *Ph.D. Thesis*, Laval University, 2000.

[2] D. Grenier, F. Labrique, H. Buyse, and E. Matagne, *Electromécanique Convertisseur d'énergie et Actionneur*, Dunod, 2001.

[3] M. Pinard, *Commande Electronique Des Moteurs Electriques*, Dunod, 2004.

[4] A. Hansen, P. Sørensen, L. Hansen, and H. Bindner, "Models for a stand-alone PV system," *Risø National Laboratory*, Roskilde, December 2000.

[5] R. Krishnan, "Electric motor drives modeling, analysis, and control," Virginia Tech, Blacksburg, VA.

[6] J. C. Balda and P. Pillay, "Speed controller design for a vector-controlled permanent magnet synchronous motor drive with parameter variations," *Industry Applications Society Annual Meeting*, 1990. Conference Record of the 1990 IEEE.

APPLIED COMPUTATIONAL ELECTROMAGNETICS SOCIETY EXPRESS JOURNAL
http://aces-society.org

INFORMATION FOR AUTHORS

PUBLICATION CRITERIA

Each paper is required to manifest some relation to applied computational electromagnetics. **Papers may address general issues in applied computational electromagnetics, or they may focus on specific applications, techniques, codes, or computational issues.** While the following list is not exhaustive, each paper will generally relate to at least one of these areas:

1. **Code validation.** This is done using internal checks or experimental, analytical or other computational data. Measured data of potential utility to code validation efforts will also be considered for publication.

2. **Code performance analysis.** This usually involves identification of numerical accuracy or other limitations, solution convergence, numerical and physical modeling error, and parameter tradeoffs. However, it is also permissible to address issues such as ease-of-use, set-up time, run time, special outputs, or other special features.

3. **Computational studies of basic physics.** This involves using a code, algorithm, or computational technique to simulate reality in such a way that better, or new physical insight or understanding, is achieved.

4. **New computational techniques** or new applications for existing computational techniques or codes.

5. **"Tricks of the trade"** in selecting and applying codes and techniques.

6. **New codes, algorithms, code enhancement, and code fixes.** This category is self-explanatory, but includes significant changes to existing codes, such as applicability extensions, algorithm optimization, problem correction, limitation removal, or other performance improvement. **Note: Code (or algorithm) capability descriptions are not acceptable, unless they contain sufficient technical material to justify consideration.**

7. **Code input/output issues.** This normally involves innovations in input (such as input geometry standardization, automatic mesh generation, or computer-aided design) or in output (whether it be tabular, graphical, statistical, Fourier-transformed, or otherwise signal-processed). Material dealing with input/output database management, output interpretation, or other input/output issues will also be considered for publication.

8. **Computer hardware issues.** This is the category for analysis of hardware capabilities and limitations of various types of electromagnetics computational requirements. Vector and parallel computational techniques and implementation are of particular interest.

Applications of interest include, but are not limited to, antennas (and their electromagnetic environments), networks, static fields, radar cross section, inverse scattering, shielding, radiation hazards, biological effects, biomedical applications, electromagnetic pulse (EMP), electromagnetic interference (EMI), electromagnetic compatibility (EMC), power transmission, charge transport, dielectric, magnetic and nonlinear materials, microwave components, MEMS, RFID, and MMIC technologies, remote sensing and geometrical and physical optics, radar and communications systems, sensors, fiber optics, plasmas, particle accelerators, generators and motors, electromagnetic wave propagation, non-destructive evaluation, eddy currents, and inverse scattering.

Techniques of interest include but not limited to frequency-domain and time-domain techniques, integral equation and differential equation techniques, diffraction theories, physical and geometrical optics, method of moments, finite differences and finite element techniques, transmission line method, modal expansions, perturbation methods, and hybrid methods.

Where possible and appropriate, authors are required to provide statements of quantitative accuracy for measured and/or computed data. This issue is discussed in "Accuracy & Publication: Requiring, quantitative accuracy statements to accompany data," by E. K. Miller, ACES Newsletter, Vol. 9, No. 3, pp. 23-29, 1994, ISBN 1056-9170.

SUBMITTAL PROCEDURE

All submissions should be uploaded to ACES server through ACES web site (http://aces-society.org) by using the upload button, Express Journal section. Only pdf files are accepted for submission. The file size should not be larger than 6MB, otherwise permission from the Editor-in-Chief should be obtained first. Automated acknowledgment of the electronic submission, after the upload process is successfully completed, will be sent to the corresponding author only. It is the responsibility of the corresponding author to keep the remaining authors, if applicable, informed. Email submission is not accepted and will not be processed.

EDITORIAL REVIEW

In order to ensure an appropriate level of quality control, papers are peer reviewed. They are reviewed both for technical correctness and for adherence to the listed guidelines regarding information content and format.

PAPER FORMAT

Only camera-ready electronic files are accepted for publication. The term **"camera-ready" means that the material is neat, legible, reproducible, and in accordance with the final version format listed below.**

The following requirements are in effect for the final version of an ACES Express Journal paper:

1. The paper title should not be placed on a separate page. The title, author(s), abstract, and (space permitting) beginning of the paper itself should all be on the first page. The title, author(s), and author affiliations should be centered (center-justified) on the first page. The title should be of font size 14 and bolded, the author names should be of font size 12 and bolded, and the author affiliation should be of font size 10 (regular font, neither italic nor bolded).

2. An abstract is required. The abstract should be a brief summary of the work described in the paper. It should state the computer codes, computational techniques, and applications discussed in the paper (as applicable) and should otherwise be usable by technical abstracting and indexing services. The word "Abstract" has to be placed at the left margin of the paper, and should be bolded and italic. It also should be followed by a hyphen (–) with the main text of the abstract starting on the same line.

3. All section titles have to be centered and all the title letters should be written in caps. The section titles need to be numbered using roman numbering (I. II. ….)

4. Either British English or American English spellings may be used, provided that each word is spelled consistently throughout the paper.

5. Internal consistency of references format should be maintained. As a guideline for authors, we recommend that references be given using numerical numbering in the body of the paper (with numerical listing of all references at the end of the paper). The first letter of the authors' first name should be listed followed by a period, which in turn, followed by the authors' complete last name. Use a comma (,) to separate between the authors' names. Titles of papers or articles should be in quotation marks (" "), followed by the title of the journal, which should be in italic font. The journal volume (vol.), issue number (no.), page numbering (pp.), month and year of publication should come after the journal title in the sequence listed here.

6. Internal consistency shall also be maintained for other elements of style, such as equation numbering. Equation numbers should be placed in parentheses at the right column margin. All symbols in any equation have to be defined before the equation appears or right immediately following the equation.

7. The use of SI units is strongly encouraged. English units may be used as secondary units (in parentheses).

8. Figures and tables should be formatted appropriately (centered within the column, side-by-side, etc.) on the page such that the presented data appears close to and after it is being referenced in the text. When including figures and tables, all care should be taken so that they will appear appropriately when printed in black and white. For better visibility of paper on computer screen, it is good to make color figures with different line styles for figures with multiple curves. Color should also be tested to insure their ability to be distinguished after black and white printing. Avoid the use of large symbols with curves in a figure. It is always better to use different line styles such as solid, dotted, dashed, etc.

9. A figure caption should be located directly beneath the corresponding figure, and should be fully justified.

10. The intent and meaning of all text should be clear. For authors who are not masters of the English language, the ACES Editorial Staff will provide assistance with grammar (subject to clarity of intent and meaning). However, this may delay the scheduled publication date.

11. Unused space should be minimized. Sections and subsections should not normally begin on a new page.

ACES reserves the right to edit any uploaded material, however, this is not generally done. It is the author(s) responsibility to provide acceptable camera-ready files in pdf and MSWord formats. Incompatible or incomplete files will not be processed for publication, and authors will be requested to re-upload a revised acceptable version.

COPYRIGHTS AND RELEASES

Each primary author must execute the online copyright form and obtain a release from his/her organization vesting the copyright with ACES. Both the author(s) and affiliated organization(s) are allowed to use the copyrighted material freely for their own private purposes.

Permission is granted to quote short passages and reproduce figures and tables from an ACES Express Journal issue provided the source is cited. Copies of ACES Express Journal articles may be made in accordance with usage permitted by Sections 107 or 108 of the U.S. Copyright Law. The consent does not extend to other kinds of copying, such as for general distribution, for advertising or promotional purposes, for creating new collective works, or for resale. The reproduction of multiple copies and the use of articles or extracts for commercial purposes require the consent of the author and specific permission from ACES. Institutional members are allowed to copy any ACES Express Journal issue for their internal distribution only.

PUBLICATION CHARGES

There is a $200 basic publication charge assigned to each paper for ACES members, and $300 charge for non-ACES members. Corresponding authors should be active members of the society at the time of submission and the time of publication in order to receive the reduced charge.

ACES Express Journal doesn't allow for more than four pages. All authors must comply with the page limitations. ACES Express Journal is an online journal, and printed copies are not available.

Upon completion of its first year, ACES Express Journal will be abstracted in INSPEC, in Engineering Index, DTIC, Science Citation Index Expanded, the Research Alert, and to Current Contents/Engineering, Computing & Technology.